

Lattice Boltzmann Study of the Steady-State Relative Permeabilities in Porous Media

Zhisheng Lv and Haibo Huang*

Department of Modern Mechanics, University of Science and Technology of China, Hefei, Anhui 230026, China

Received 19 May 2020; Accepted (in revised version) 24 June 2020

Abstract. A multiple-relaxation-time (MRT) lattice Boltzmann model (LBM) is used to study the relative permeabilities in porous media. In many simulations in the literature, usually the periodic boundary condition at inlet and outlet and a uniform pressure gradient were applied to measure the relative permeabilities. However, it is not consistent with the pressure or velocity boundary conditions in the real experiments and may lead to unphysical results. Here using the convective outflow and constant velocity boundary conditions at outlet and inlet, respectively, we can simulate the real experimental setup. Meanwhile, the distribution of the two phases at the outlet can be resolved. The effects of wettability, initial saturation, viscosity ratio ($M \in (1, 50)$), capillary number ($Ca \in (10^{-4}, 10^{-2})$) and micro two-phase distribution at the inlet on permeabilities are investigated comprehensively. It is found that generally speaking, the strong wetting, drainage, larger Ca , and larger M may result in a larger relative permeability of the non-wetting phase. Different flow pattern, the lubrication effect of the wetting phase that attaches to the wall, and influence of stagnant pores may contribute to the feature. The study is helpful to further develop the LBM to simulate the real experimental process.

AMS subject classifications: 76S05, 76T99, 76M28

Key words: Lattice Boltzmann, multiphase, convective outflow, porous media, relative permeabilities.

1 Introduction

Numerical study of multiphase flow in porous media is of great benefit to engineering applications [1–3]. Numerous macroscopic numerical methods have been developed for solving the two-phase Navier-Stokes (N-S) equation [4], such as the front-tracking method, volume-of-fluid (VOF) method, level set method, and so on. The former three

*Corresponding author.

Email: huanghb@ustc.edu.cn (H. B. Huang)

methods are the most popular ones. However, the front-tracking method is usually difficult to simulate interface coalescence or break-up [4, 5]. In the VOF and level set methods, usually the interface reconstruction step or the interface reinitialization is required, which may be non-physical or complex to implement [5]. Besides, numerical instability may appear when the VOF and level set methods are applied to simulate surface-tension-dominated flows in complex geometries [4].

In the last twenty years, the Lattice Boltzmann method (LBM) has been developed into a useful tool to solve two-phase flow in porous media [6–11]. The LBM is a mesoscopic method and easy to handle complex wall geometries. It is also an explicit method, which makes the code easy to parallelize. In the LBM, solving the Poisson equation is not required. Hence, it is more efficient than common macroscopic schemes.

There are many multiphase LBMs available in the literature [7]. However, quantitative numerical study shows that the Rothman and Keller (R-K) model is more accurate than the other models [12]. The model was firstly proposed by Rothman and Keller [13] and further developed by Gunstensen et al. [14] through introducing an extra binary fluid collision into the Lattice Boltzmann equation [14]. Latva-Kokko and Rothman [15] improved the recoloring step in the R-K model, which is able to reduce the lattice pinning effect and decrease the spurious currents [5, 16]. Now the recoloring step is widely used in applications of the R-K model [5, 12, 17]. Recently, Reis and Phillips developed a two-dimensional nine-velocity R-K model [18]. In the model, a revised binary fluid collision is proposed and is shown to be able to recover the additional term which accounts for surface tension in the N-S equation [18].

For the R-K model, the wetting condition, i.e., contact angle in the pore scale can be specified through setting the densities of the two fluids in the solid nodes. That is more simpler than its counterpart, the free-energy LB model, in which the gradient of the density near the wall has to be imposed. Due to this simplicity, the model has been applied to simulations of multiphase flows in porous media [8, 19]. Reducing spurious currents is another important issue for multiphase models. Here in the R-K method, the multiple-relaxation-time (MRT) collision model [20] is adopted. The present method is able to reduce spurious currents and improve numerical stability significantly. Those are good features for reproducing the capillary fingering phenomena for two-phase flow in porous media [21].

There are many numerical simulations for testing the relative permeability, e.g., [11, 22, 23]. That is very different from the measurement scheme in experiments. Due to periodic boundary condition, the flow at the outlet is supposed to flow back to the inlet boundary. In this setup, the porous media is supposed to be infinitely long in the flow direction. That is different from the reality. Besides, the relative permeability has been reported to be slightly negative in the preliminary results of [11, 23, 24], which is not physically valid. These values are likely a result of applying periodic boundary conditions to a nonperiodic porous medium [23].

Hence, non-periodic boundary conditions may be necessary to develop. In [25], two-phase immiscible displacements driven by constant pressure difference were simulated.

The pressure outlet boundary condition is somewhat similar to that in [26]. However, the performance of the boundary condition seems not good because in Fig. 2 in [26], when a droplet is close to the outlet it deforms severely.

In reality, the porous medium is located between the inlet and outlet boundaries, in which the wetting and non-wetting fluids are injected into the inlet by pumps and flow out at the outlet. Usually the pressure sensors are located close to the inlet and outlet boundary. At the steady state, When the flow flux and saturation in the porous media become statistically steady, through measuring the pressure drop and flow flux of each phase, we are able to obtain the relative permeability.

Hence, it is important to simulate the realistic flow in the experimental setup. In the setup, the free outflow boundary condition has to be developed to handle the flow at the outlet. The boundary condition should be able to determine the phase distribution at the outlet automatically. The convective outflow boundary condition [27,28] may be able to fulfill this task.

Here using the convective outflow boundary and inlet constant flux boundary condition, in our simulations the setup of real measurement of the relative permeabilities is recovered. The effects of wettability, initial saturation, viscosity ratio ($M \in (1,50)$), capillary number ($Ca \in (10^{-4}, 10^{-2})$) and micro two-phase distribution at the inlet on permeabilities are investigated comprehensively.

The paper is arranged in the following way. First the present R-K model and the convective outflow boundary condition are introduced. The numerical method is also validated through two benchmark problems. Then a 400×400 porous media is introduced in our simulations. Relative permeability variation due to the wetting property, initial saturation, capillary number and viscosity ratio are investigated comprehensively. Finally, relevant mechanisms for these effects are explored.

2 Method

2.1 R-K model

In the R-K model, the particle distribution function (PDF) for fluid k is defined to be f_i^k . For two-phase flows, two distribution functions are defined, i.e., f_i^b and f_i^r , where b and r denote "blue" and "red" component, respectively. The total PDF at (\mathbf{x}, \mathbf{t}) is $f_i(\mathbf{x}, \mathbf{t}) = \sum_k f_i^k(\mathbf{x}, \mathbf{t})$.

Usually there are two steps implemented in the LBM, collision and streaming. In the R-K model, there are three steps for each component: streaming, collision, and recoloring. Suppose an iteration begins from the streaming step. We illustrate how the three steps construct a loop. The streaming step is [18]

$$f_i^k(\mathbf{x} + \mathbf{e}_i \delta t, t + \delta t) = f_i^{k+}(\mathbf{x}, t), \quad (2.1)$$

where f_i^{k+} is the PDF after the recoloring step. In the above equation, $\mathbf{e}_i, i = 0, 1, \dots, b$ are the discrete velocities of the velocity models. For the D2Q9 velocity model ($b = 8$). Here c

is the lattice speed defined to be $c = \frac{\delta x}{\delta t}$. We use the lattice units of $1l.u. = 1\delta x$, $1t.s. = 1\delta t$, and the mass unit is $m.u.$ in our study.

The collision step can be written as [15]

$$f_i^{k*}(\mathbf{x}, t) = f_i^k(\mathbf{x}, t) + (\Omega_i^k)^1 + (\Omega_i^k)^2, \quad (2.2)$$

where $f_i^{k*}(\mathbf{x}, t)$ is the post-collision state. There are two collision terms in the equation, i.e., $(\Omega_i^k)^1$ and $(\Omega_i^k)^2$. If the lattice BGK scheme is adopted, the first collision term is

$$(\Omega_i^k)^1 = -\frac{\delta t}{\tau} \left(f_i^k(\mathbf{x}, t) - f_i^{k,eq}(\mathbf{x}, t) \right), \quad (2.3)$$

where τ is the relaxation time.

The equilibrium distribution function $f_i^{k,eq}(\mathbf{x}, t)$ can be calculated using [18]

$$f_i^{k,eq}(\mathbf{x}, t) = \rho_k \left(C_i + w_i \left[\frac{\mathbf{e}_i \cdot \mathbf{u}}{c_s^2} + \frac{(\mathbf{e}_i \cdot \mathbf{u})^2}{2c_s^4} - \frac{(\mathbf{u})^2}{2c_s^2} \right] \right), \quad (2.4)$$

where the density of the k th component is

$$\rho_k = \sum_i f_i^k, \quad (2.5)$$

and the total density is $\rho = \sum_k \rho_k$. The momentum is

$$\rho \mathbf{u} = \sum_k \sum_i f_i^k \mathbf{e}_i. \quad (2.6)$$

In the above formula, the coefficients are [18] $C_0 = \alpha_k$, $C_i = \frac{1-\alpha_k}{5}$, $i=1,2,3,4$ and $C_i = \frac{1-\alpha_k}{20}$, $i=5,6,7,8$, where α_k is a parameter that is assumed able to adjust the density of fluids [18,29] but it may be not true [30]. The other parameters are $w_0 = \frac{4}{9}$, $w_i = \frac{1}{9}$, $i=1,2,3,4$, and $w_i = \frac{1}{36}$, $i=5,6,7,8$.

When the relaxation time parameters for the two fluids are very different, for example, $\tau_r = 0.501$ and $\tau_b = 1.0$, $\tau(\mathbf{x})$ at the interface can be determined by a simple way: if

$$\psi(\mathbf{x}) = \frac{\rho_r(\mathbf{x}) - \rho_b(\mathbf{x})}{\rho_r(\mathbf{x}) + \rho_b(\mathbf{x})} > 0,$$

$\tau(\mathbf{x}) = \tau_r$ and otherwise $\tau(\mathbf{x}) = \tau_b$. To make the relaxation parameter ($\tau(\mathbf{x})$) change smoothly at the interfaces between two fluids, the interpolation scheme constructed by Grunau et al. [18,29] is an alternative way. In our simulations, the simple way is adopted. The viscosity of each component is $\nu_k = c_s^2(\tau_k - 0.5)$, where $c_s^2 = \frac{1}{3}c^2$. The viscosity ratio is defined as $M = \frac{\nu_n}{\nu_w}$, where the subscript "n", "w" denote the non-wetting fluid and wetting fluid, respectively.

The second collision term is more complex and there are some different forms found in the literature [11,18]. An example is [11]:

$$(\Omega_i^k)^2 = \frac{A}{2} |\mathbf{f}| (2 \cdot \cos^2(\lambda_i) - 1), \quad (2.7)$$

where λ_i is the angle between the color gradient \mathbf{f} and the direction \mathbf{e}_i , and we have $\cos(\lambda_i) = \frac{\mathbf{e}_i \cdot \mathbf{f}}{|\mathbf{e}_i| |\mathbf{f}|}$ [15].

The color-gradient $\mathbf{f}(\mathbf{x}, t)$ is calculated as [15]:

$$\mathbf{f}(\mathbf{x}, t) = \sum_i \mathbf{e}_i \sum_j [f_j^r(\mathbf{x} + \mathbf{e}_i \delta t, t) - f_j^b(\mathbf{x} + \mathbf{e}_i \delta t, t)]. \tag{2.8}$$

However, according to the study of Reis and Phillips [18], the correct collision operator should be

$$(\Omega_i^k)^2 = \frac{A}{2} |\mathbf{f}| \left[w_i \frac{(\mathbf{e}_i \cdot \mathbf{f})^2}{|\mathbf{f}|^2} - B_i \right], \tag{2.9}$$

where $B_0 = -\frac{4}{27}$, $B_i = \frac{2}{27}$, $i=1,2,3,4$, $B_i = \frac{5}{108}$, $i=5,6,7,8$. Using these parameters, the correct term due to surface tension in the N-S equation can be recovered [18].

Then the recoloring step is implemented to achieve separation of the two fluids [15],

$$f_i^{r,+} = \frac{\rho_r}{\rho} f_i^* + \beta \frac{\rho_r \rho_b}{\rho^2} f_i^{(eq)}(\rho, 0) \cos(\lambda_i), \tag{2.10a}$$

$$f_i^{b,+} = \frac{\rho_b}{\rho} f_i^* - \beta \frac{\rho_r \rho_b}{\rho^2} f_i^{(eq)}(\rho, 0) \cos(\lambda_i), \tag{2.10b}$$

where $f_i^* = \sum_k f_i^{k*}$.

After $f_i^r(\mathbf{x}, t)$ and $f_i^b(\mathbf{x}, t)$ are updated, the streaming steps (i.e., Eq. (2.1)) should be implemented for each component. Through iteration of the procedure illustrated above, two-phase flows can be simulated.

In the model, A and β are the two most important parameters that adjust interfacial properties. β does not change the surface tension but affects the interface thickness, isotropy, and the magnitude of spurious current [21]. Usually β is chosen to be 0.5 in our simulations [21]. The surface tension is only determined by τ_r , τ_b and A [15]. The surface tension σ as a function of A for the R-K simulations with viscosity ratio $M = 1$ can be determined analytically [18]. Later Huang et al. [21] have shown that over a wide range of M , σ is also proportional to the parameter A , i.e., $\sigma = 2.72A$. The pressure in the flow field can be obtained from the density via the equation of state $p = c_s^2 \rho$.

In our study, only components with identical densities are considered and the corresponding equilibrium PDF is Eq. (2.4) with $C_i = w_i$. That is the common equilibrium PDF usually used in the LBM [31]. Hence, for two components with identical densities, the equilibrium PDF has the same formula. It is not necessary to calculate both collision step Eq. (2.3) and Eq. (2.9) separately for each component. The two collision steps become

$$(\Omega_i)^1 = -\frac{\delta t}{\tau} (f_i(\mathbf{x}, t) - f_i^{eq}(\mathbf{x}, t)), \tag{2.11a}$$

$$(\Omega_i)^2 = A |\mathbf{f}| \left[w_i \frac{(\mathbf{e}_i \cdot \mathbf{f})^2}{|\mathbf{f}|^2} - B_i \right], \tag{2.11b}$$

where $f_i = \sum_k f_i^k$.

2.2 MRT R-K model

The difference between the MRT and BGK R-K model is the collision term. The collision term $(\Omega_i)^1$ in Eq. (2.11a) should be replaced by the MRT collision model [20]. That is

$$(\Omega_i)^1 = -M^{-1} \hat{\mathbf{S}} \left[|m(\mathbf{x}, \mathbf{t})\rangle - |m^{(eq)}(\mathbf{x}, \mathbf{t})\rangle \right], \quad (2.12)$$

where the Dirac notation of ket $|\cdot\rangle$ vectors symbolize column vectors. The collision matrix $\hat{\mathbf{S}} = M \cdot \mathbf{S} \cdot M^{-1}$ is diagonal with $\hat{\mathbf{S}} = \text{diag}(s_0, s_1, \dots, s_b)$. $|m^{(eq)}\rangle$ is the equilibrium value of the moment $|m\rangle$. The matrix M [20] is a linear transformation which is used to map a vector $|f\rangle$ in discrete velocity space to a vector $|m\rangle$ in moment space, i.e., $|m\rangle = M \cdot |f\rangle$, $|f\rangle = M^{-1} \cdot |m\rangle$.

The momenta $j_\zeta = \rho u_\zeta$ are obtained from

$$j_\zeta = \sum_i f_i e_{i\zeta}, \quad (2.13)$$

where ζ denotes x or y coordinates. The collision process is executed in moment space [20]. For the D2Q9 model, $|m\rangle = (\rho, e, \epsilon, j_x, q_x, j_y, q_y, p_{xx}, p_{xy})^T$, where e , ϵ , and q_ζ are the energy, the energy square, and the heat flux, respectively.

$$|m^{(eq)}\rangle = (\rho, e^{eq}, \epsilon^{eq}, j_x^{eq}, q_x^{eq}, j_y^{eq}, q_y^{eq}, p_{xx}^{eq}, p_{xy}^{eq})^T,$$

where

$$\begin{aligned} e^{eq} &= -2\rho + 3(j_x^2 + j_y^2) / \rho, & \epsilon^{eq} &= \rho - 3(j_x^2 + j_y^2) / \rho, & q_x^{eq} &= -j_x, \\ q_y^{eq} &= -j_y, & p_{xx}^{eq} &= (j_x^2 - j_y^2) / \rho, & p_{xy}^{eq} &= j_x j_y / \rho. \end{aligned}$$

The diagonal collision matrix $\hat{\mathbf{S}}$ is given by [20] $\hat{\mathbf{S}} \equiv \text{diag}(s_0, s_1, s_2, s_3, s_4, s_5, s_6, s_7, s_8)$. The parameters are chosen as: $s_0 = s_3 = s_5 = 1.0$, $s_1 = 1.64$, $s_2 = 1.54$, $s_4 = s_6 = 1.9$, and $s_7 = s_8 = \frac{1}{\tau}$. Compared to the BGK R-K model, the MRT R-K model decreases the spurious current significantly at high viscosity contrast [21].

2.3 Contact angle

To consider the effect of wettability on the relative permeability, we have to specify the contact angle in the pore scale. Through setting ρ_r and ρ_b values on the wall nodes, i.e., ρ_{wr} and ρ_{wb} , different contact angles can be specified. The contact angle θ can be analytically determined by [15]

$$\theta = \arccos\left(\frac{\rho_{wr} - \rho_{wb}}{\rho_i}\right), \quad (2.14)$$

where θ is measured from the red phase. In this way, the wetting property of the wall can be specified because ρ_{wr} and ρ_{wb} affect the color gradient illustrated in Eq. (2.8).

2.4 Boundary conditions

When simulate the immiscible displacements, the velocity inlet boundary condition and constant pressure (or density) boundary condition can be set for the upper and lower boundary, respectively. In the upper boundary the PDF f_4, f_7, f_8 are unknown after the streaming step for the non-wetting fluid (majority component). Through non-equilibrium bounce back assumption [26], one gets the density of the majority component is

$$\rho_n = \frac{f_0^n + f_1^n + f_3^n + 2(f_2^n + f_5^n + f_6^n)}{1 + u_i}, \quad (2.15)$$

and the unknowns can be obtained through [26]

$$f_4^n = f_2^n - \frac{2}{3}\rho_n u_i, \quad (2.16a)$$

$$f_7^n = f_5^n + \frac{1}{2}(f_1^n - f_3^n) - \frac{1}{6}\rho_n u_i, \quad (2.16b)$$

$$f_8^n = f_6^n + \frac{1}{2}(f_3^n - f_1^n) - \frac{1}{6}\rho_n u_i, \quad (2.16c)$$

where u_i is the specified inlet velocity of the non-wetting fluid.

The pressure boundary conditions for the lower boundary can be handled similarly [26]. Suppose ρ_s is the density of the wetting component (majority component) that is specified on the lower convective outlet boundary node. One can get the outlet velocity of wetting fluid

$$u_y = 1 - \frac{f_0^w + f_1^w + f_3^w + 2(f_4^w + f_7^w + f_8^w)}{\rho_s}, \quad (2.17)$$

and the unknowns are

$$f_2^w = f_4^w + \frac{2}{3}\rho_s u_y, \quad (2.18a)$$

$$f_5^w = f_7^w + \frac{1}{2}(f_3^w - f_1^w) + \frac{1}{6}\rho_s u_y, \quad (2.18b)$$

$$f_6^w = f_8^w + \frac{1}{2}(f_1^w - f_3^w) + \frac{1}{6}\rho_s u_y. \quad (2.18c)$$

We note that maintaining the density (or pressure) of the minority component, which is usually set to be a very small value, say $10^{-8}m.u./l.u.^3$, on both the upper and lower boundaries is also important.

In the setup for measuring relative permeabilities, however the constant pressure boundary condition is difficult to determine a lattice node on the outlet is occupied by the red or blue component. It maybe reasonable to perform an extrapolation. For example, if the node that one or two layers above the bottom boundary, is red, it is reasonable to assume the node will be occupied by the red component. Then the density of the red

is specified for the node, the minor density is specified for the other component. However, the simple extrapolation does not work well because the outflow sometimes seems blocked at the lower boundary.

To make the fluid flow out the the domain naturally, for the lower outflow boundary condition, the convection boundary condition is imposed [27,28], i.e.,

$$\frac{\partial \chi}{\partial t} + U_i \frac{\partial \chi}{\partial y} = 0, \quad (2.19)$$

where U_i is the convective velocity, χ represents any physical variables we used in our simulations [28]. In our simulations at the outlet $j=1$ the convective velocity in the lattice (i,j) is specified as that in the upper neighbouring layer, i.e., $U_i = u_y(i, j+1)$.

In the layer $j=1$, suppose $\chi = f_i$ if the upwind scheme is used, we have

$$\frac{f_k^n(j) - f_k^{n-1}(j)}{\Delta t} + U_i \frac{f_k^n(j+1) - f_k^n(j)}{\Delta y} = 0 \quad (2.20)$$

for $U_i < 0$. It yield

$$f_k^n(j) = \left[\frac{\Delta y}{\Delta t} f_k^{n-1}(j) - U_i f_k^n(j+1) \right] / \left(\frac{\Delta y}{\Delta t} - U_i \right), \quad (2.21)$$

where $k=0,1,\dots,8$ and $j=1$. On the other hand, if $U_i > 0$ and upwind scheme is applied, it means that the information transfers from the outside of the domain into the domain. Since the information from outside is unknown, we simply set $U_i = 0$ for the case $U_i > 0$, i.e., $f_k^n(j) = f_k^{n-1}(j)$ is applied. In the follows we would test how the boundary condition works.

3 Numerical validations

To validate the out-flow boundary condition, first a two-phase displacement case is simulated. The result is shown in Fig. 1. In this case, the computational domain is $400lu \times 540lu$. The density ratio is unity and viscosity ratio of red and blue phase is 10 ($\tau_r = 1.5$, $\tau_b = 0.6$). The upper velocity boundary condition is specified [26] and the constant displacing velocity is $-0.01l.u./t.s$. The lower outflow boundary condition is applied. Periodic boundary condition is applied to the left and right boundaries. From Fig. 1, It is seen that the upper blue phase displaces the red phase containing a blue-phase bubble. In the procedure, the blue-phase bubble passes the bottom boundary smoothly without deformation. The interface moves seamlessly through the outflow and open boundary. Finally it thoroughly leaves the computational domain. It is seen that in the simulation, the phase distribution at the lower boundary is convected from the inner upper lattices due to convection boundary condition.

To further validate the boundary condition, another simulation was also performed and compared with the experimental result in [32]. The porous medium consists many

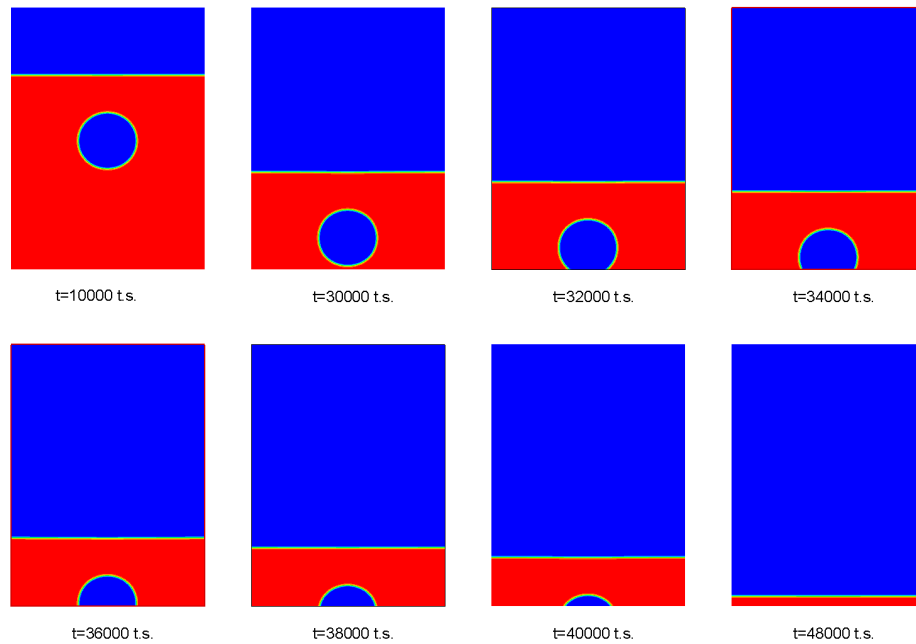


Figure 1: Two-phase displacement. The upper blue phase displaces the red phase containing a blue-phase droplet. Displacing velocity is $-0.011u/ts$. Density ratio is unity and viscosity ratio of red and blue phase is 10. Periodic boundary condition is applied to the left and right boundaries.

identical cylinders with irregular spacings (see Fig. 2). The key physical parameters of the porous medium and those for the wetting and non-wetting fluids in the experiment are listed in the right-most column in Table 1 [32]. The parameters in the LBM simulation are also listed in Table 1.

Table 1: Geometrical parameters and fluid properties in the LB simulation and experiment.

	Symbol	Simulation	Experiment
Model length	L	600	30mm
Model width	W	600	30mm
Obstacle diameter	b	42	2mm
Porosity	ϕ	≈ 0.59	≈ 0.59
Single-phase permeability	k	≈ 17	$2.1 \times 10^{-4} \text{cm}^2$
Contact angle	θ_w	$\approx 40^\circ$	$< 70^\circ$
Wetting fluid viscosity	μ_w	1/3	$3.6 \times 10^{-3} \text{Pa}\cdot\text{s}$
Non-wetting fluid viscosity	μ_{nw}	1/3	$1.9 \times 10^{-5} \text{Pa}\cdot\text{s}$
Wetting fluid density	ρ_w	1.0	$1.10 \times 10^3 \text{kg}\cdot\text{m}^{-3}$
Non-wetting fluid density	ρ_{nw}	1.0	$1.2 \text{kg}\cdot\text{m}^{-3}$
Surface tension	σ	0.108	$\approx 6.2 \times 10^{-2} \text{N}\cdot\text{m}^{-1}$
Capillary number	Ca	$\approx 3.2 \times 10^{-2}$	$\approx 2.6 \times 10^{-5}$

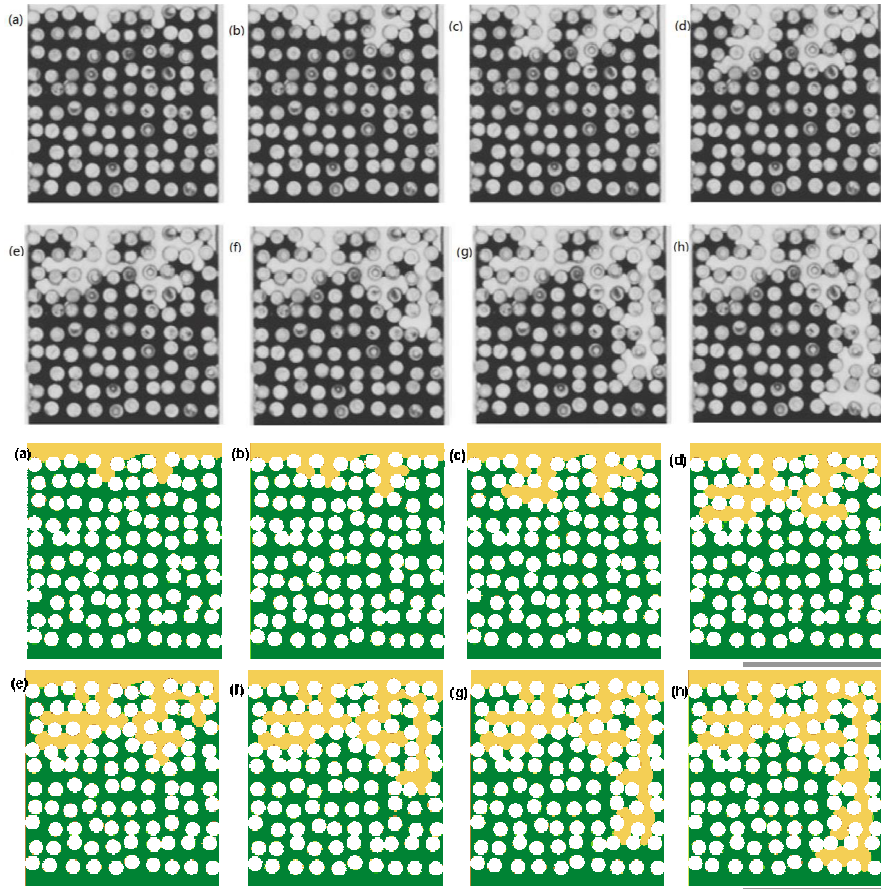


Figure 2: Initially wetting phase -saturated porous media displaced by the a non-wetting fluid. The result of the LBM simulation (the lower two rows (a)-(h)) is compared the experimental result (the upper two rows (a)-(h)) in [32].

In the simulation, a $600lu \times 600lu$ domain is used to discretize the porous medium. The obstacle diameter is 42 lattice units. The porous media has porosity of 0.59. Both the non-wetting and wetting fluids have density of unity and at solid nodes $\rho_r = 0.7$, $\rho_b = 0.0$. The corresponding contact angle of the wetting red phase is about 40° (see Eq. (2.14)). The relaxation times for the two fluids are $\tau_r = \tau_b = 1.0$ and the two fluids have identical viscosity. $A = 0.04$ and the corresponding surface tension is $\sigma \approx 2.72 \times A = 0.108$. Hence it is seen that in the LBM simulation viscosity ratio M is unity while in the experiment is about 5.27×10^{-3} . Besides M , another key parameter is the capillary number, Ca , which on pore scale is defined as $Ca = \frac{\mu_w b^2 u_0}{k\sigma}$, where u_0 is the average inlet velocity. The Ca numbers in our simulation and the experiment [32] are approximately 3.2×10^{-2} and 2.6×10^{-5} , respectively. According to phase diagram in [33], at small M and small Ca the flow pattern may be viscous fingering. In our simulation, we tried to minimize the

capillary number. However, when Ca is too small, numerical instability may appear. Hence, after a trial and error test, the smallest Ca in this simulation that we are able to achieve is about $\sim 3.2 \times 10^{-2}$, which is adopted in this validation case. According to [33], in the M - Ca plane, the viscous fingering pattern covers a wide range. Although the Ca number in our simulation is not so small as that in the experiment, the flow pattern may be still the viscous fingering. Two flows with same pattern may look like very much. Hence, our simulation and the experiment may be still comparable.

In the experiment in [32], the invasion process in the experiment is driven by a constant invasion rate. However, in their LBM simulation [32], instead applying a constant inlet velocity boundary condition, they adopt a body force $F(t)$, which is fluctuating in time, acting globally on the whole system. In their simulation, the fluctuating manner of the body force is similar to that measured in the experiment. In this way, the constant invasion rate may be recovered from the LBM simulation. It is seen that this boundary condition depends on the pressure history measured in the experiment. It is not a priori and not so straightforward.

In our simulation a constant inlet velocity boundary condition with $u_0 = 10^{-4}lu/ts$ is applied. At the lower boundary condition the outflow boundary condition is adopted. In the displacement simulation, initially the non-wetting fluid occupies at least 10 layer lattices near the upper inlet boundary. From Fig. 2, it is seen that phase distributions in our LBM result ((a)-(h) in the lower two rows) are consistent with those in the experiment ((a)-(h) in the upper two rows), respectively. Hence, the convective boundary condition is further validated.

4 Immiscible two-phase flow in porous media

In this section, two-phase flow in a porous medium is simulated. A typical apparatus used to measure the relative permeabilities in the experiment is shown in Fig. 3(a). At the inlet, the two phases are injected through 15 syringes simultaneously. The pressures close to the inlet and outlet are measured by pressure sensors.

Our simulation setup is shown in Fig. 3(b). It shows an initial condition of our simulations. The red, green and black regions represent the nonwetting phase (NWP), wetting phase (WP) and solid, respectively. At the inlet, the NWP or WP are injected into the 25 channels at a constant flow rate, which is similar to the situation in the experiment. In our simulations, there are blank section between the inlet and porous region. In this way, they are able to mix before they enter the porous region. The free outflow condition is applied at the outlet. The blank section between the outlet and porous region is set to avoid the capillary end effect at the outlet, which may cause numerical instability. The left and right sides of the domain are periodic. The pressures close to the inlet and outlet of the porous are monitored in our simulation. Hence, our simulation setup is very similar to the experimental process of measuring relative permeability in the laboratory.

Porous medium structure generations are not a topic we are concerned with here.

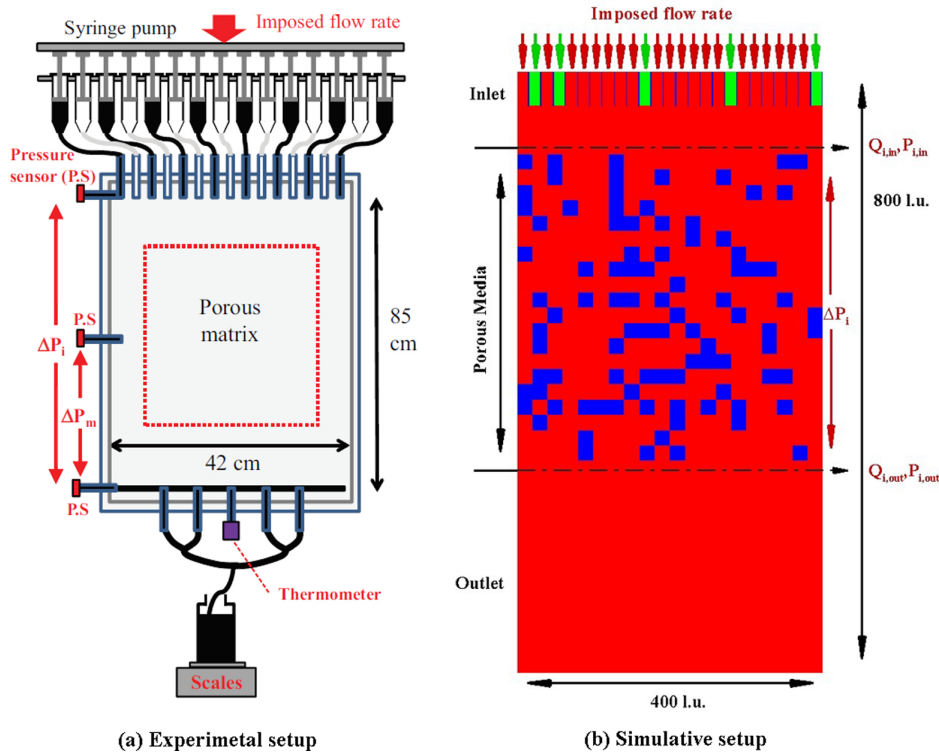


Figure 3: (a) Sketch of experimental setup from the work of Erpelding et al. [35]. The two phases are contained in 15 syringes, each connected to one of the 15 inlet nodes of the porous model (seven syringes of air represented in white and eight syringes of water glycerol solution in black). The same syringe pump is used to inject both phases simultaneously. The dotted lines give the dimensions of the area studied by image analysis. (b) An initial condition of simulation in our works. In the $400 \times 800 lu^2$ domain, the blue regions represent solid while the red, green and blue regions stand for the NWP, WP, and solid, respectively. Periodic boundary condition is applied to the left and right boundaries. The velocity boundary condition and the free outflow boundary condition are applied at the upper inlet and the lower outlet, respectively.

The porous medium in [34] is adopted in our simulations, which is a 2D pore networks of $20^2 lu^2$ square solid and void pore space blocks. The porosity of the network is 0.776. The size of the whole network is $400 \times 400 lu^2$. The absolute permeability of the porous medium is $48.8 l.u.^2$, which is determined by single-phase lattice Boltzmann simulations. In our simulations, the flow region is initially occupied by one component. At every flow node, the dominating and the minority component have densities of $1.0 m.u./l.u.^3$ and $10^{-8} m.u./l.u.^3$, respectively. Although the densities of the two fluids are identical, the kinematic viscosity can be adjusted to achieve different dynamic viscosity ratio. The wettability of the solid can be set through specifying ρ_{wb} and ρ_{wr} (see Section 2.3).

In our cases, the inlet velocity has magnitude of $10^{-4} \sim 10^{-3} lu/ts$. In our study, the capillary number (Ca) and the viscosity ratio (M) are two key dimensionless numbers. The capillary number is defined as $Ca = \frac{Q_w \mu_w}{\sigma A_0}$, where Q_w is the flow flux of the wetting component, A_0 is the area of the cross section of the porous media. For the 2D porous

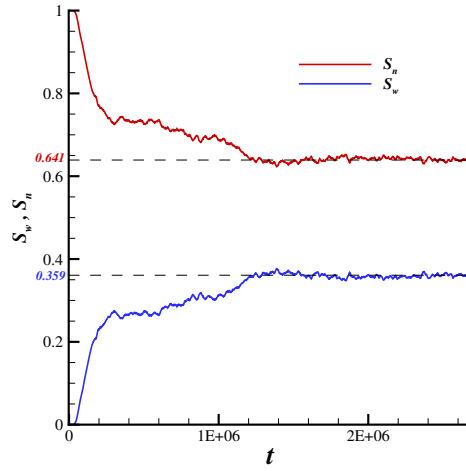


Figure 4: Phase saturations (S_w, S_n) as functions of time (t) for a simulation case with $Ca = 0.02$.

media in our simulation, $A_0 = 400lu$.

In our simulations, the relative permeabilities of two phases are calculated by Darcy’s law, i.e.,

$$k_{r,i} = \frac{Q_i \mu_i \Delta L}{KA_0 \Delta P_i}, \quad (i = w, n), \tag{4.1}$$

where Q_i is the flow flux of the WP or NWP at the cross section, μ_i the viscosity of the WP or NWP, K the absolute permeability, ΔL the length of the porous media and $\Delta P_i = P_{i,in} - P_{i,out}$ the pressure drop of the WP or NWP between the inlet and the outlet. Our simulations are run until steady states achieved, at which the wetting saturation S_w is almost a constant (see Fig. 4). Then the flow flux and the pressure drop (see Fig. 3(b)) at steady state are calculated. Finally, the relative permeabilities are obtained using Eq. (4.1).

Next, we study the effect of wettability, initial saturation, capillary number, and viscosity ratio ($M = \frac{\mu_n}{\mu_w}$) on the relative permeability. In the following simulations, to fix Ca and achieve different saturation, the WP occupies 5 channels and the WP inlet velocity $u_{w,in}$ is fixed but the inlet velocity of the NWP at the other 20 inlet channels $u_{n,in}$ varies (see Fig. 3(b)).

4.1 Wettability effect

To investigate the wettability effect, simulations of two group cases were carried out. The parameters in the two groups are shown in Table 2. It is seen that in all cases, the NWP is more viscous than the WP because $\tau_n = 1.5$ and $\tau_w = 0.6$. In all cases, the porous media is initially saturated with the NWP. The capillary numbers of all cases have the same magnitude of 10^{-3} .

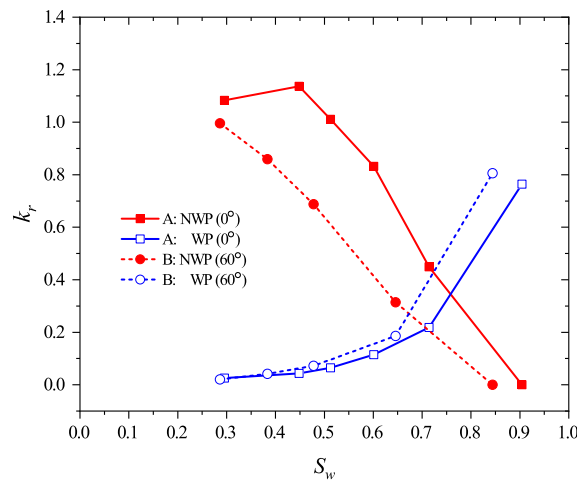


Figure 5: Relative permeability as function of saturation of the WP (S_w) for simulations *A* and *B*. Filled and hollow symbols denote relative permeabilities of NWP and WP, respectively. Key parameters for simulations *A* and *B* are listed in Table 2. "0°" and "60°" in the legend denote the static contact angles of the WP in simulations *A* and *B*, respectively. Each point represents a case in our simulation. In the simulations $Ca=0.002$.

Table 2: Two group cases for investigation of wettability effect on k_r .

group	contact angle of the WP	initial phase	τ_n (NWP)	τ_w (WP)	Ca	M	description
A	0°	NWP	1.5	0.6	0.002	10	strong wetting
B	60°	NWP	1.5	0.6	0.002	10	neutrally wetting

Fig. 5 shows k_r as functions of saturation of the WP (S_w) for group *A* and *B*. The filled and hollow squares represent $k_{r,n}$ (k_r of the NWP) and $k_{r,w}$ (k_r of the WP), respectively. It is seen that generally speaking, $k_{r,w}$ increases with S_w while $k_{r,n}$ decreases with S_w . The trend is reasonable because when there are more WP in the porous media, the WP may be more continuous and $k_{r,w}$ should be high. It is also noticed that for group *A*, $k_{r,n}$ may exceed unity. Because when S_w is small, the WP mainly attaches the solid walls, which acts like a moisture. The attached WP is less viscous and helps the NWP flow faster in the pores and the NWP would be easier to penetrate the porous media. Hence, $k_{r,n}$ is larger than any single phase case, e.g., the non-wetting fluid itself.

From Fig. 5, it is also seen that strong wetting cases have a larger $k_{r,n}$ and smaller $k_{r,w}$ than the neutrally wetting cases at a specific saturation. In order to figure out the effect of wettability, phase distributions in the porous media at the steady state for typical cases with $S_w \approx 0.6$ in group *A* and *B* are shown in Figs. 6(a) and (b), respectively. From Fig. 6(a), it is seen that the NWP forms two connected paths and occupies the center of the two main paths. While in the neutrally wetting case, the NWP forms only one connected path (see Fig. 6(b)). Besides, Fig. 6(a) shows that in the strong wetting case, the WP is always attached to the wall (see the marked regions 1, 2 and 3). The WP acts as moisture,

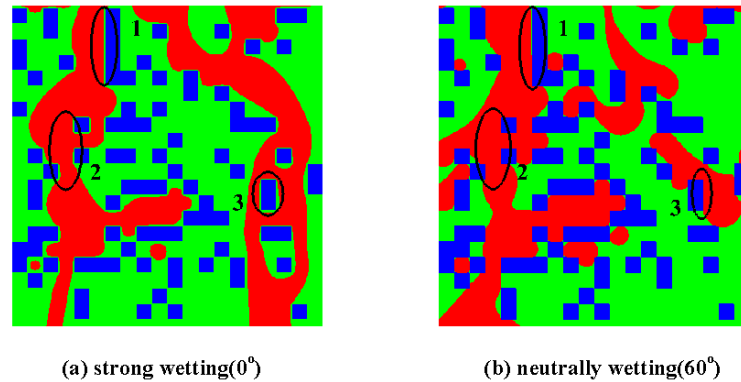


Figure 6: Instantaneous phase distributions of (a) the strong wetting (0°) case with $S_w=0.601$ and (b) the neutrally wetting (60°) case with $S_w=0.646$. The red, green and blue regions stand for the NWP, WP, and solid, respectively.

which helps the NWP flow faster in the pores. While in the neutrally wetting case (see Fig. 6(b)), the NWP is attached to the wall directly (see the marked regions 1, 2 and 3). Hence, at a specific S_w , the strong wetting case has a larger $k_{r,n}$.

On the other hand, the flow in main channels significantly affects k_r of two phases, due to the parabolic velocity profile in the channel. Compared to the strong wetting case, the WP in the neutrally wetting case has more opportunities to flow at the center of the main channels. Hence, the WP may flow faster in the neutrally wetting case. In this way, the neutrally wetting case has a higher $k_{r,w}$ at a specific S_w .

4.2 Initial saturation effect

In this section, we study the effect of initial saturation on relative permeability by simulating two group cases, including drainage and imbibition. Imbibition refers to a displacement process in a porous media which is initially saturated by the NWP. On the other hand, if the porous media is initially saturated by the WP, the flow process is called drainage. To investigate the initial saturation effect, the porous media in group A and B are initially filled with the NWP and WP, respectively (see Table 3).

Fig. 7 shows k_r as a function of S_w for group A and B. The filled and hollow squares represent $k_{r,n}$ and $k_{r,w}$, respectively. It should be noted that the curves represent different

Table 3: Two group cases for investigation of initial saturation effect on k_r .

group	initial phase	contact angle of the WP	τ_n	τ_w	Ca	M	description
A	WP	0°	1.5	0.6	0.002	10	drainage
B	NWP	0°	1.5	0.6	0.002	10	imbibition

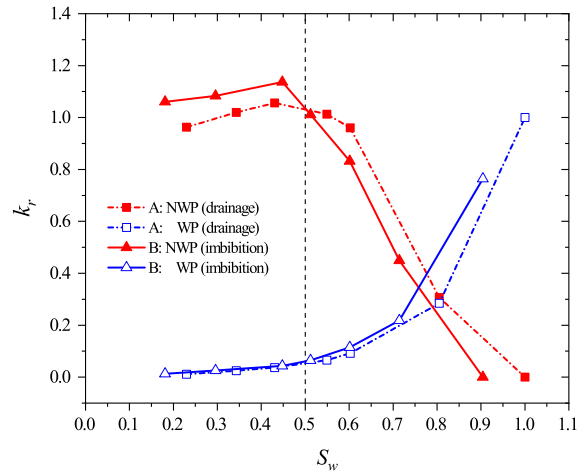


Figure 7: k_r as a function of S_w (saturation of the WP) for simulations A and B for investigation of initial saturation effect. Filled and hollow symbols denote $k_{r,n}$ and $k_{r,w}$, respectively. Key parameters for simulations A and B are listed in Table 3. The vertical dashed black line is set at $S_w=0.5$, which separates the curves into two sides. The curves in different sides represent different laws. In the simulations $Ca=0.002$.

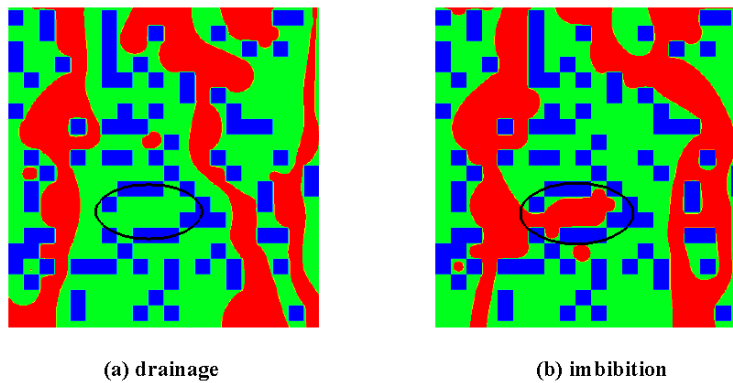


Figure 8: An instantaneous phase distribution of (a) a drainage case with $S_w=0.602$ and (b) an imbibition case with $S_w=0.601$. The red, green and blue regions represent the NWP, WP and solid, respectively. The marked region shows the stagnant pores.

features in the two sides of the vertical dashed black line. In the left side ($S_w < 0.5$), $k_{r,n}$ of drainage is smaller than that of imbibition, and $k_{r,w}$ of two processes approximately equal, at the same saturation. However, in the right side ($S_w > 0.5$), $k_{r,n}$ of drainage is larger than that of imbibition, while $k_{r,w}$ of drainage is smaller than that of imbibition, at a specific S_w .

To find out the effect of initial saturation, phase distributions in the porous media at the steady state for typical cases with $S_w \approx 0.6$ in group A and B are shown in Figs. 8(a)

Table 4: Three group cases for investigation of capillary number effect on k_r .

group	Ca	contact angle of WP	initial phase	τ_n	τ_w	M
A	0.02	0°	NWP	1.5	0.6	10
B	0.002	0°	NWP	1.5	0.6	10
C	0.0002	0°	NWP	1.5	0.6	10

and (b), respectively. It is seen that the main difference between Figs. 8(a) and (b) lies in phase distribution in the dead-end pores (see the marked region). In the drainage and imbibition cases, the marked dead-end pore is filled with the WP and NWP, respectively. Therefore in the imbibition case, a part of the NWP is stagnant in the dead-end pore and the effective saturation of the NWP is smaller than it appears. Smaller effective saturation usually leads to smaller permeability. Hence, when $S_w > 0.5$, $k_{r,n}$ of drainage is larger than that of imbibition and meanwhile $k_{r,w}$ of drainage is smaller than that of imbibition.

When S_w is small ($S_w < 0.5$), the lubrication effect of the WP makes the NWP easy to flow through the porous media. However, a part of the WP is trapped in the stagnant pores in drainage, and thus the lubrication effect would be weakened. Therefore, $k_{r,n}$ of drainage is smaller than that of imbibition at a $S_w < 0.5$. When S_w is small, the WP mainly attaches to the wall and are disconnected. Hence $k_{r,w}$ is close to zero.

4.3 Capillary number effect

To study capillary number (Ca) effect on k_r , we implement three group simulations which are controlled with the same conditions except Ca . The Ca is defined as $Ca = \frac{Q_w \mu_w}{\sigma A}$. As mentioned above, our model allows us to simulate cases with different surface tension. Here, Ca can be changed by setting surface tension σ and flow flux Q_w . In the three group simulations, the wettability, the initial saturation and M of the two phases are identical.

It is seen from Fig. 9 that Ca has a significant effect on both $k_{r,n}$ and $k_{r,w}$. Besides, $k_{r,n}$ and $k_{r,w}$ both get smaller as Ca decreases, at a specific saturation. Fig. 10 shows $\frac{k_{r,n}}{k_{r,w}}$ as a function of S_w . It is seen that the ratio $\frac{k_{r,n}}{k_{r,w}}$ becomes larger when Ca decreases at $S_w < 0.6$ although at a small Ca , both $k_{r,n}$ and $k_{r,w}$ are small. These results agree well with those obtained by Blunt et al. [36] using network modeling.

In order to further understand the effect of Ca , the instantaneous phase distributions of the cases of $Ca = 0.02$ and $Ca = 0.0002$ for $S_w \approx 0.7$ are shown in Figs. 11(a) and (b), respectively. For comparison, several regions are labeled in (a) and (b). It is seen that at $Ca = 0.02$, the NWP is easy to deform and pinch off due to the relatively smaller σ . This is advantageous for both two phases to flow because the two phases may coflow in a flow path. Consequently, at large Ca , both phases have relatively larger permeabilities while $\frac{k_{r,n}}{k_{r,w}}$ may be not so significant as that at small Ca at a specific S_w (see Fig. 10).

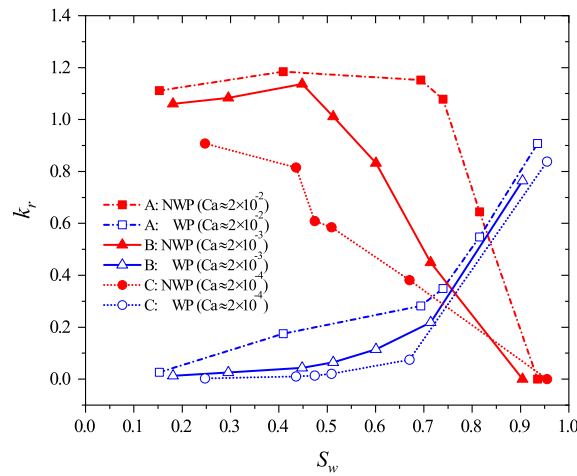


Figure 9: Relative permeability as function of saturation of wetting phase (S_w) for simulations A , B and C for investigation of capillary number effect. Filled and hollow symbols denote $k_{r,n}$ and $k_{r,w}$, respectively. Key parameters for simulations A , B and C are listed in Table 4.

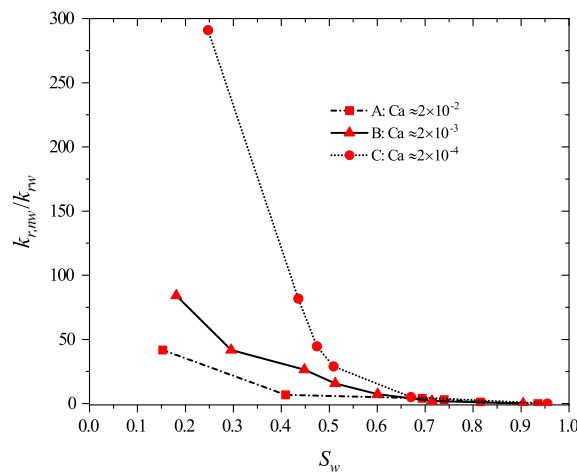


Figure 10: Relative permeability ratio as function of S_w for simulations A , B and C for different Ca .

On the other hand, at $Ca = 0.0002$, the NWP is able to maintain its shape and not easy to be pinched off (see Fig. 11(b)). the feature helps the NWP to occupy the main flow paths and make it more connected. Consequently, at small Ca , the WP flow may be significantly blocked by the NWP. As a result, the ratio $\frac{k_{r,n}}{k_{r,w}}$ becomes larger at a specific saturation (see Fig. 10).

It is also seen that the NWP in the black circles in (b) is stuck and unable to flow due to the large capillary resistance in the narrow pores. So at small Ca , the NWP is easier to be trapped and the flow paths may be blocked, which reduces the flow capacity of both

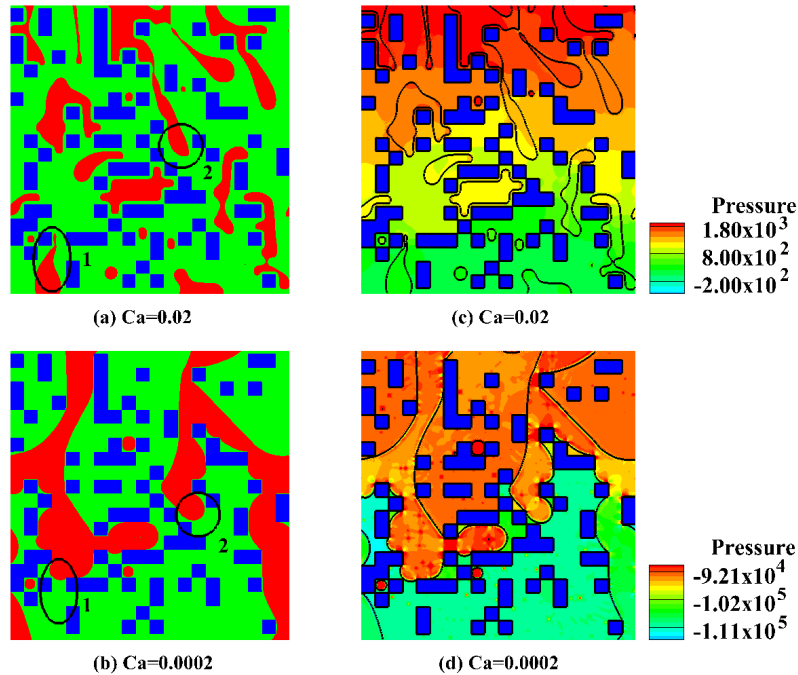


Figure 11: An instantaneous phase distribution of (a) a $Ca = 0.02$ case with $S_w = 0.69$ (b) a $Ca = 0.0002$ case with $S_w = 0.67$. The blue, red and the green regions represent solid, NWP and WP, respectively. (c) and (d) are the pressure contours of (a) and (b), respectively. In (c) and (d), the black lines denote the interfaces between the WP and NWP.

phases. Therefore, both $k_{r,n}$ and $k_{r,w}$ at small Ca is smaller than those at large Ca for a specific S_w .

The above issue can also be understood from the nondimensional pressure distribution in the porous media (Figs. 11(c) and (d)). The nondimensional equation is $p^* = \frac{p - c_s^2 \rho}{\rho U^2}$, where $U = \frac{Q_w}{A}$ is the characteristic velocity. The maximum pressure drop in Fig. 11(c) is approximately 2×10^3 , and that in (d) is 2×10^4 . Hence, the pressure drop in the case of $Ca = 0.0002$ is much larger than that in the case $Ca = 0.02$. In Fig. 11(d), it is also seen that the pressure drop at the interface between the WP and NWP is remarkable, which implies the NWP may be difficult to overcome the capillary resistance. While in the case of $Ca = 0.02$ (Fig. 11(c)), due to small capillary force, the pressure drops at the interface between the WP and NWP is small.

4.4 Viscosity ratio effect

To find out the viscosity ratio effect on relative permeability, three group cases with different M were simulated. The capillary numbers of all cases have the same magnitude of 10^{-3} . The parameters are shown in Table 5.

Table 5: Three group cases for investigation of viscosity ratio effect on k_r .

group	M	contact angle of the WP	initial phase	τ_n	τ_w	Ca
A	1	0°	WP	1.0	1.0	0.002
B	10	0°	WP	1.5	0.6	0.002
C	50	0°	WP	1.5	0.52	0.002

From Fig. 12, it is seen that a higher M leads to a higher $k_{r,n}$ at a specific S_w . It also shows that $k_{r,w}$ becomes smaller as M increases at a specific S_w . Our results about the effect of M on k_r are consistent with those obtained by Blunt et al. [36] using network model. To further understand the effect of M , the instantaneous phase distribution of two cases with $M=1$ and $M=10$ are illustrated in Fig. 13.

As mentioned before, the WP tends to attach the solid walls and acts like a moisture (see Section 4.1). Figs. 13(c) and (d) present the velocity fields of the $M=1$ and $M=10$ cases, respectively. In both cases, $S_w \approx 0.4$. Overall the velocity fields in Figs. 13(c) and (d) have the same order of magnitude. From the zoom-in views, we find that the velocities of the NWP at $M=1$ and $M=10$ have the same order of magnitude. According to $k_{r,n} = \frac{Q_n \mu_n \Delta L}{KA \Delta P_n}$, the $k_{r,n}$ would increase with increasing μ_n when Q_n and ΔP_n are constant. It is noted that ΔP_n in the cases $M=1$ and $M=10$ is close. Therefore at higher M , $k_{r,n}$ becomes larger at a specific saturation (see Fig. 12). Similarly, $k_{r,n}$ of the cases with $M=50$ is usually larger than that in the cases with $M=10$ at a specific S_w .

According to [37], when $Ca > 10^{-5}$ and $M > 1$, viscous fingering pattern may occur in the two-phase flow in the porous media. It is seen from the marked regions 1 and 3 in

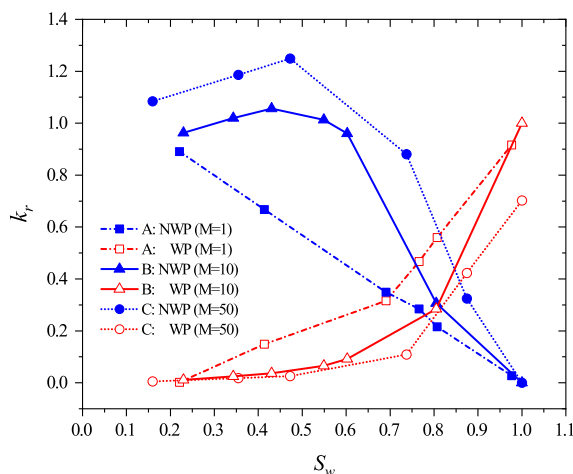


Figure 12: Relative permeability as function of S_w for simulations A, B and C, for different M . Filled and hollow symbols denote $k_{r,n}$ and $k_{r,w}$, respectively. Key parameters for simulations A, B and C are listed in Table 5.

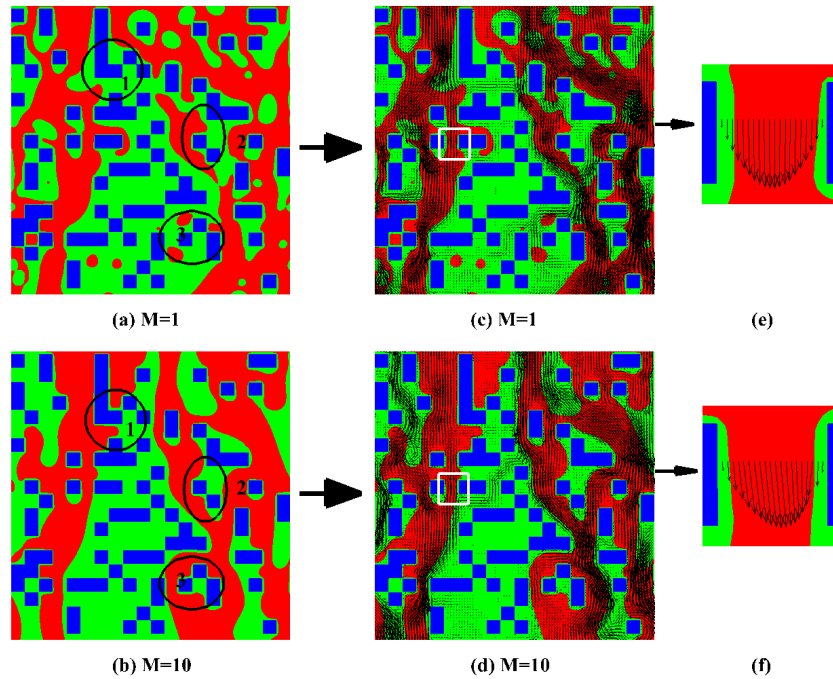


Figure 13: Instantaneous phase distribution for (a) a $M=1$ case with $S_w=0.414$ and (b) a $M=10$ case with $S_w=0.405$. (c) and (d) the velocity fields of (a) and (b), respectively. (e)-(f) zoom-in view of the white square regions in (c) and (d), respectively.

Fig. 13(b) that more WP may be trapped by the NWP at larger M and the WP becomes more difficult to flow. Therefore, $k_{r,w}$ becomes smaller when M is larger at a specific S_w (see Fig. 12).

4.5 Effect of two-phase distribution at the inlet

Two-phase distribution at the inlet may influence the measured k_r . To evaluate the effect, here two groups of simulations (Cases A and B) with different phase distribution at the inlet are performed. The physical parameters in the ten cases are $\tau_n=1.5$, $\tau_w=0.6$, $u_{w,in}=0.001$, $u_{n,in}=0.001$, $\sigma=2.79 \times 10^{-3}$ and $\theta=0^\circ$.

The phase distributions at the inlet 25 channels for cases with $S_w \approx 30\%$ and 60% are shown in Table 6. The letter "N" and "W" represent the NWP and WP, respectively. It is seen that the phase distributions at the inlet 25 channels in Case A and Case B are significantly different although they lead to almost identical S_w . For the case of $S_w \approx 5\%$, only one of the 25 inlet channels is filled with the WP. For the cases of $S_w \approx 80\%$, and 85% only two and one inlet channel are filled with the NWP, respectively. In the

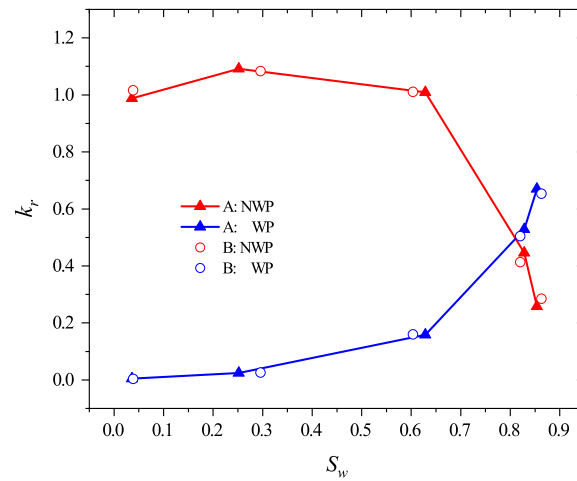


Figure 14: Relative permeabilities as functions of S_w for simulations A and B with different phase distributions at the inlet. Filled and hollow symbols denote $k_{r,n}$ and $k_{r,w}$, respectively. Distributions at the inlet for $S_w \approx 30\%$ and 60% are listed in Table 6.

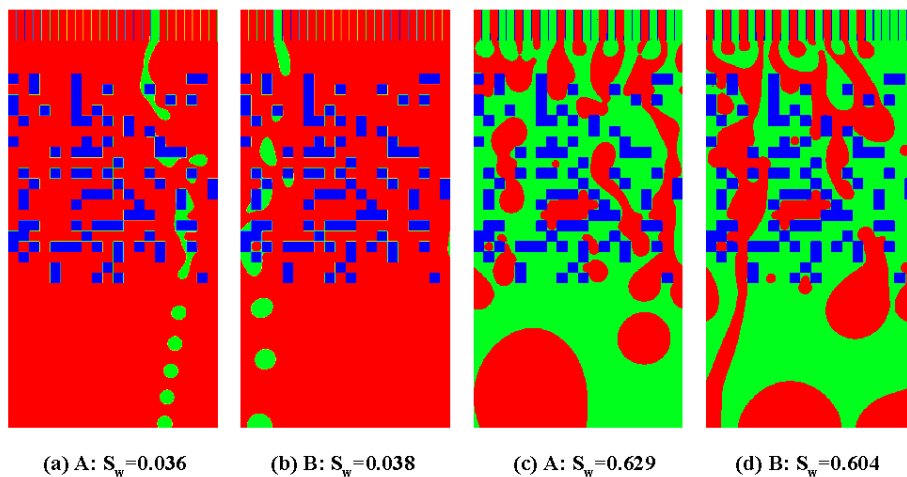


Figure 15: Instantaneous phase distributions at steady state for four cases with (a) $S_w = 0.036$ (Group A), (b) $S_w = 0.038$ (Group B), (c) $S_w = 0.629$ (Group A) and (d) $S_w = 0.604$ (Group B), respectively. In the cases $Ca = 0.002$.

corresponding Cases A and B, the inlet channels mentioned in the cases of $S_w \approx 5\%$, 80% , 85% are located close to the right and left boundaries, respectively. For the resultant relative permeabilities, Fig. 14 shows that $k_{r,w}$ and $k_{r,n}$ at five specified saturations ($S_w \approx 5\%$, 30% , 60% , 80% , 85%) of Case B (circles) are all very close to those of Case A (triangles).

Fig. 15 shows the two-phase distribution at the inlet and the resultant instantaneous distribution in the porous medium at steady state for cases with $S_w \approx 3.8\%$ and 60% .

Table 6: The phase distributions at the inlet for cases with $S_w \approx 30\%$ and 60% .

S_w	group	distributions of inlet channels (N: NWP, W: WP)	inlet number (N: W)
$\approx 30\%$	A	NNNNNNNNNWNWNNNNNNNWNWNNNNW	20: 5
$\approx 30\%$	B	NWNNWNNNNNNWNNNNNNNWNNNNNNW	20: 5
$\approx 60\%$	A	NWNNWNNWNNWNNWNNWNNWNNWNNWNNWNNWNNW	10: 15
$\approx 60\%$	B	NWNNWNNWNNWNNWNNWNNWNNWNNWNNWNNWNNW	10: 15

It is seen from Figs. 15(a) and (b) that both flows of the WP are not so continuous and their flow paths are located in the right and left main passages, respectively due to the locations of the WP at the inlet. Since the flows seem similar, $k_{r,w}$ s in Case A and B are close, so do $k_{r,n}$ s. From Fig. 15(c), we can see that the flow in the left main path is not continuous while that in the right path is continuous. The situation in Fig. 15(d) is reversed. Overall, the penetration abilities of the NWP in the porous media in Case A and B are close. Hence, $k_{r,n}$ s in Case A and B are close, so do $k_{r,w}$ s.

In summary, the distribution only has very minor effect on k_r . The possible reasons are listed in follows. First, although the porous media is not homogeneous, it has two main paths in the left and right part, respectively. In other words, the porous media is close to homogeneous and not so heterogeneous. Second, the two phases are mixed in some extent before they enter the porous region. The two features weaken the effect of phase distribution at the inlet.

5 Conclusions

The R-K model is developed to simulate the relative permeability measurement in reality. This distinctive feature of experimental self-determined outflow two-phase distribution at the outlet is reproduced in the LBM simulations by the convective boundary condition.

Using the R-K model, we implement a series of simulations to investigate the effects of wettability, initial condition, Ca and M on the relative permeabilities. Our analysis can be summarized as follows:

- (a) The strong wetting cases have a larger $k_{r,n}$ than the neutrally wetting cases at a specific S_w due to the more opportunity to flow in the middle of the channel and the lubrication effect of the WP that attaches to the wall. Besides, $k_{r,n}$ may exceed unity at smaller S_w .
- (b) At $Ca \approx 10^{-3}$, compared to the drainage process, $k_{r,n}$ of the imbibition is smaller at $S_w > 0.5$ because a part of the NWP is stagnant in the dead-end pore and the effective saturation of the NWP is smaller than it appears. At $S_w < 0.5$, $k_{r,n}$ of the drainage is lower, because a part of the WP is trapped in the stagnant pores in drainage, which weakens the lubrication effect.

- (c) As Ca decreases, capillary fingering is more and more dominated, in which more WP would be trapped in small pore and the flow paths may be blocked. Meanwhile, the NWP has more opportunity to be connected in large pores. As results, the relative permeabilities of both two phases decrease, but $\frac{k_{r,n}}{k_{r,w}}$ rises.
- (d) When M increases, more micro fingers are generated, which results in a smaller $k_{r,w}$. At a high M and smaller S_w , the lubrication effect of the WP is remarkable.

This study provides a more realistic LBM simulation setup for measuring relative permeability in porous media and predicting the two-phase flow in porous media.

Acknowledgements

This work was supported by the National Science Foundation of China (NSFC, Grant No. 11472269).

References

- [1] Y.-R. YUAN, A.-J. CHENG, AND C.-F. LI, *A characteristics-mixed volume element method for the displacement problem of enhanced oil recovery*, Adv. Appl. Math. Mech., 11(5) (2019), pp. 1084–1113.
- [2] S. HUSSAIN, *Finite element solution for mhd flow of nanofluids with heat and mass transfer through a porous media with thermal radiation, viscous dissipation and chemical reaction effects*, Adv. Appl. Math. Mech., 9(4) (2018), pp. 904–923.
- [3] Y.-X. WANG, X.-F. HAN, AND Z.-Y. SI, *A viscosity-splitting method for the Navier-Stokes/Darcy problem*, Adv. Appl. Math. Mech., 12(1) (2019), pp. 251–277.
- [4] R. SCARDOVELLI AND S. ZALESKI, *Direct numerical simulation of free-surface and interfacial flow*, Annu. Rev. Fluid Mech., 31(1) (1999), pp. 567–603.
- [5] H.-H. LIU, A. J. VALOCCHI, AND Q.-J. KANG, *Three-dimensional lattice Boltzmann model for immiscible two-phase flow simulations*, Phys. Rev. E, 85(4) (2012), 046309.
- [6] A. D. ANGELOPOULOS, V. N. PAUNOV, V. N. BURGANOS, AND A. C. PAYATAKES, *Lattice Boltzmann simulation of nonideal vapor-liquid flow in porous media*, Phys. Rev. E, 57(3) (1998), pp. 3237.
- [7] M. C. SUKOP AND D. T. THORNE, *Lattice Boltzmann Modeling: An Introduction for Geoscientists and Engineers*, Berlin: Springer, 2005.
- [8] K. LANGAAS AND P. PAPTZACOS, *Numerical investigations of the steady state relative permeability of a simplified porous medium*, Transp. Porous Media, 45(2) (2001), pp. 241–266.
- [9] C. PAN, M. HILPERT, AND C. T. MILLER, *Lattice-Boltzmann simulation of two-phase flow in porous media*, Water Resour. Res., 40(1) (2004).
- [10] J. F. CHAU AND D. OR, *Linking drainage front morphology with gaseous diffusion in unsaturated porous media: a lattice Boltzmann study*, Phys. Rev. E, 74(5) (2006), 056304.
- [11] H.-B. HUANG AND X.-Y. LU, *Relative permeabilities and coupling effects in steady-state gas-liquid flow in porous media: a lattice Boltzmann study*, Phys. Fluids, 21(9) (2009), 092104.
- [12] H.-B. HUANG, L. WANG, AND X.-Y. LU, *Evaluation of three lattice Boltzmann models for multiphase flows in porous media*, Comput. Math. Appl., 61(12) (2011), pp. 3606–3617.

- [13] D. H. ROTHMAN AND J. M. KELLER, *Immiscible cellular-automaton fluids*, J. Stat. Phys., 52(3-4) (1988), pp. 1119–1127.
- [14] A. K. GUNSTENSEN, D. H. ROTHMAN, S. ZALESKI, AND G. ZANETTI, *Lattice Boltzmann model of immiscible fluids*, Phys. Rev. A, 43(8) (1991), pp. 4320.
- [15] M. LATVA-KOKKO AND D. H. ROTHMAN, *Static contact angle in lattice Boltzmann models of immiscible fluids*, Phys. Rev. E, 72(4) (2005), 046701.
- [16] S. LECLAIRE, M. REGGIO, AND J.-Y. TRÉPANIÉ, *Numerical evaluation of two recoloring operators for an immiscible two-phase flow lattice Boltzmann model*, Appl. Math. Model., 36(5) (2012), pp. 2237–2252.
- [17] M. LATVA-KOKKO AND D. H. ROTHMAN, *Scaling of dynamic contact angles in a lattice-Boltzmann model*, Phys. Rev. Lett., 98(25) (2007), pp. 254503.
- [18] T. REIS AND T. N. PHILLIPS, *Lattice Boltzmann model for simulating immiscible two-phase flows*, J. Phys. A Math. Theor., 40(14) (2007), pp. 4033.
- [19] J. TÖLKE, *Lattice Boltzmann simulations of binary fluid flow through porous media*, Philos. T. R. Soc. A., 360(1792) (2002), pp. 535–545.
- [20] P. LALLEMAND AND L.-S. LUO, *Theory of the lattice Boltzmann method: dispersion, dissipation, isotropy, galilean invariance, and stability*, Phys. Rev. E, 61(6) (2000), pp. 6546.
- [21] H.-B. HUANG, J.-J. HUANG, AND X.-Y. LU, *Study of immiscible displacements in porous media using a color-gradient-based multiphase lattice Boltzmann method*, Comput. Fluids, 93 (2014), pp. 164–172.
- [22] H. LI, C. PAN, AND C. T. MILLER, *Pore-scale investigation of viscous coupling effects for two-phase flow in porous media*, Phys. Rev. E Stat. Nonlin. Soft Matter Phys., 72(2) (2005), 026705.
- [23] C. J. LANDRY, Z. T. KARPYN, AND O. AYALA, *Relative permeability of homogenous-wet and mixed-wet porous media as determined by pore-scale lattice Boltzmann modeling*, Water Resour. Res., 50(5) (2014), pp. 3672–3689.
- [24] E. S. BOEK AND M. VENTUROLI, *Lattice-Boltzmann studies of fluid flow in porous media with realistic rock geometries*, Comput. Math. Appl., 59(7) (2010), pp. 2305–2314.
- [25] J.-W. HUANG, F. XIAO, AND X.-L. YIN, *Lattice Boltzmann simulation of pressure-driven two-phase flows in capillary tube and porous medium*, Comput. Fluids, 155 (2017), pp. 134–145.
- [26] Q.-S. ZOU AND X.-Y. HE, *On pressure and velocity boundary conditions for the lattice Boltzmann bgc model*, Phys. Fluids, 9(6) (1997), pp. 1591–1598.
- [27] A. FAKHARI, Y.-F. LI, D. BOLSTER, AND K. T. CHRISTENSEN, *A phase-field lattice Boltzmann model for simulating multiphase flows in porous media: application and comparison to experiments of CO₂ sequestration at pore scale*, Adv. Water Resour., 114 (2018), pp. 119–134.
- [28] Q. LOU, Z.-L. GUO, AND B.-C. SHI, *Evaluation of outflow boundary conditions for two-phase lattice Boltzmann equation*, Phys. Rev. E, 87(6) (2013), 063301.
- [29] D. GRUNAU, S. CHEN, AND K. EGGERT, *A lattice Boltzmann model for multiphase fluid flows*, Phys. Fluids A, 5(10) (1993), pp. 2557–2562.
- [30] H.-B. HUANG, J.-J. HUANG, X.-Y. LU, AND M. C. SUKOP, *On simulations of high-density ratio flows using color-gradient multiphase lattice Boltzmann models*, Int. J. Mod. Phys. C, 24(04) (2013), 1350021.
- [31] H.-B. HUANG, D. T. THORNE, M. G. SCHAAP, AND M. C. SUKOP, *Proposed approximation for contact angles in shan-and-chen-type multicomponent multiphase lattice Boltzmann models*, Phys. Rev. E, 76(6) (2007), 066701.
- [32] O. AURSJØ, G. LØVOLL, H. A. KNUDSEN, E. G. FLEKKØY, AND K. J. MÅLØY, *A direct comparison between a slow pore scale drainage experiment and a 2d lattice Boltzmann simulation*, Transp. Porous Media, 86(1) (2011), pp. 125–134.

- [33] R. LENORMAND, E. TOUBOUL, AND C. ZARCONE, *Numerical models and experiments on immiscible displacements in porous media*, J. Fluid Mech., 189 (1988), pp. 165–187.
- [34] A. G. YIOTIS, J. PSIHOGIOS, M. E. KAINOURGIAKIS, A. PAPAIOANNOU, AND A. K. STUBOS, *A lattice Boltzmann study of viscous coupling effects in immiscible two-phase flow in porous media*, Colloids Surf., A, 300(1-2) (2007), pp. 35–49.
- [35] M. ERPELDING, S. SINHA, K. T. TALLAKSTAD, A. HANSEN, E. G. FLEKKOY, AND K. J. MALOY, *History independence of steady state in simultaneous two-phase flow through two-dimensional porous media*, Phys. Rev. E, 88(5) (2013).
- [36] M. BLUNT AND P. KING, *Relative permeabilities from two- and three-dimensional pore-scale network modelling*, Transp. Porous Media, 6(4) (1991), pp. 407–433.
- [37] R. LENORMAND, E. TOUBOUL, AND C. ZARCONE, *Numerical-models and experiments on immiscible displacements in porous-media*, J. Fluid Mech., 189 (1988), pp. 165–187.